ACS Sustainable Chemistry & Engineering

Research Article

Cite This: ACS Sustainable Chem. Eng. 2019, 7, 12170−12178

pubs.acs.org/journal/ascecg

Selective Hydrogen Evolution on Manganese Oxide Coated Electrodes: New Cathodes for Sodium Chlorate Production

Balázs Endrődi,*[,†,‡] Aleksandra Stojanovic,[†] Maria Cuartero,[§] Nina Simic,[∥] Mats Wildlock,[∥] Roland de Marco,[⊥,#] Gaston A. Crespo,[§] and Ann Cornell*[,†]

[†]Applied Electrochemistry, School of Engineering Sciences in Chemistry, Biotechnology and Health, KTH Royal Institute of Technology, Teknikringen 42, SE-100 44 Stockholm, Sweden

[‡]Department of Physical Chemistry and Materials Science, University of Szeged, Rerrich Bela Square 1, H-6720 Szeged, Hungary

[§]Department of Chemistry, School of Engineering Science in Chemistry, Biotechnology and Health, KTH Royal Institute of Technology, Teknikringen 30, SE-10044 Stockholm, Sweden

[∥]Nouryon Pulp and Performance Chemicals AB, Färjevägen 1, SE-445 80 Bohus, Sweden

[⊥]Faculty of Science, Health, Education and Engineering, University of the Sunshine Coast, Sippy Downs Drive 90, Sippy Downs, Queensland 4556, Australia

[#]School of Chemistry and Molecular Biosciences, The University of Queensland, Cooper Road 68, Brisbane, Queensland 4072, Australia

Supporting Information

ABSTRACT: The safety and feasibility of industrial electrochemical production of sodium chlorate, an important chemical in the pulp and paper industry, depend on the selectivity of the electrode processes. The cathodic reduction of anodic products is sufficiently suppressed in the current technology by the addition of chromium(VI) to the electrolyte, but due to the high toxicity of these compounds, alternative pathways are required to maintain high process efficiency. In this paper, we evaluate the electrochemical hydrogen evolution reaction kinetics and selectivity on thermally formed manganese oxide-coated titanium electrodes in hypochlorite and chlorate solutions. The morphology and phase composition of manganese oxide layers were varied via alteration of the annealing temperature during synthesis, as confirmed by scanning electron microscopy, X-ray diffraction, synchrotron radiation X-ray photoelectron spectroscopy, and near-edge X-ray absorption fine structure spectroscopy measurements. As shown in mass spectroscopy coupled electrochemical measurements, the hydrogen evolution selectivity in hypochlorite and chlorate solutions is dictated by the phase composition of the coating. Importantly, a hydrogen evolution efficiency of above 95% was achieved with electrodes of optimized composition (annealing temperature, thickness) in hypochlorite solutions. Further, these electrode coatings are nontoxic and Earth-abundant, offering the possibility of a more sustainable chlorate production.

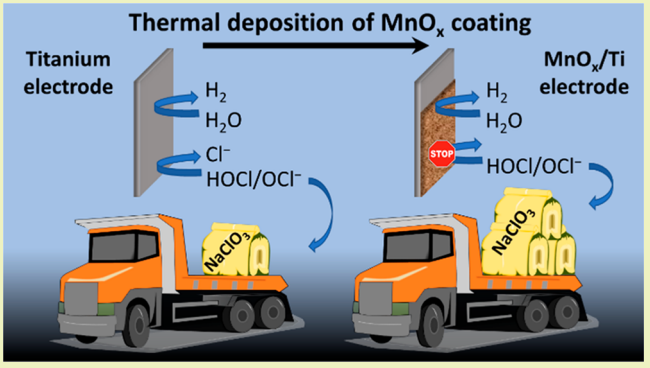

KEYWORDS: *Cathode selectivity, HER, Industrial electrochemistry, Chemical technology, Dichromate*

INTRODUCTION

The industrial production of sodium chlorate is one of the largest industrial electrochemical processes both in terms of annual production and energy consumption. Since it is the dominantly applied reagent for wood pulp bleaching, the demand for sodium chlorate is still on the rise with an ever increasing use of different paper products.[1]

During electrochemical production, a concentrated brine solution at temperatures ranging from 70 to 90 °C is electrolyzed in undivided electrochemical cells to form hydrogen on the cathode and chlorine on the anode. The latter species hydrolyses to hypochlorite, which reacts further to chlorate in the bulk electrolyte, resulting in an overall stoichiometry shown in eq 1.

$$NaCl + 3H_2O \xrightarrow{\text{electrical energy}} NaClO_3 + 3H_2 \quad (1)$$

A typical chlorate electrolyte contains about 2 mol dm^{-3} NaCl and chlorate at a concentration above 5 mol dm^{-3}, together with the chlorate-forming intermediates (e.g., hypochlorite ion and hypochlorous acid, referred to as

Received: March 4, 2019
Revised: May 14, 2019
Published: June 15, 2019

"hypochlorite" in the following text) present in a lower concentration (10−40 mmol dm^{-3}). The anodic losses due to oxygen formation are kept low by using dimensionally stable anodes (DSA), on which chlorine evolution proceeds with high selectivity.[2−5] In the undivided cells, the reduction of both chlorate and chlorate-forming intermediates on the used low-carbon steel cathodes causes significant cathodic losses. With the current technology, a high hydrogen evolution reaction (HER) selectivity is ensured by a thin chromium(III) oxide/hydroxide film, deposited during electrolysis on the cathode from the reduction of chromium(VI), dissolved in the electrolyte.[6−10] This chromium(VI) also buffers the solution[11] and increases the homogeneous chlorate formation rate[12−14] and selectivity,[15] making it a crucial component of the chlorate electrolyte, leading to an overall current efficiency of ∼95%. Due to the high toxicity of chromium(VI), there is an urgent need to find alternative solutions allowing processing at high current and energy efficiencies. This is further strengthened by a recent European Commission decision, aiming to completely phase out the use of chromium(VI) species.[16]

Several attempts have been taken to directly replace chromium(VI).[1] Alkaline and rare earth metal salts[17−19] and molybdate[20−22] were used to increase HER efficiency in dilute hypochlorite solutions, but none of these additives get close to the efficacy achieved with chromium(VI) under industrially relevant conditions. Most recently, we proved permanganate[23] and vanadate[24] to be promising alternative electrolyte additives. What is common in all of these cases (including the chromium(VI)) is the formation of an amorphous oxide/hydroxide layer on the cathode during electrolysis. While a recent study implies that the change in the reaction mechanism contributes to the increased HER selectivity,[25] it is often attributed to the selective transport of different species through the hydrated oxide/hydroxide coatings. Interestingly, similar amorphous oxide coatings were successfully applied in other research fields ranging from photocatalytic water splitting[26−28] to HER catalyst protection;[29,30] the beneficial influence of these layers was explained by the selective transport of different compounds through them. This similarity offers the possibility to use such protected cathodes in the chlorate process to avoid the unwanted reactions. So far, however, only chromium-containing cathodes were shown to achieve high selectivity during chlorate electrolysis.[25,31]

A similar selectivity is desired with seawater electrolysis, where the anodic formation of chlorine must be circumvented.[32,33] Here, anodes coated with manganese oxides allow a selectivity approaching 100% for oxygen evolution from seawater.[34−41] Again, the selectivity of the coating was explained by a mass transport phenomenon,[42,43] by hindered diffusion of species other than water and formed oxygen gas through the otherwise passive coatings.[44]

In a recent contribution, we found that amorphous, mixed-valence-state manganese oxide formed from the reduction of permanganate leads to increased HER selectivity in hypochlorite solutions.[23] However, the continuous growth of the layer was found to be a major obstacle in the industrial implementation. In this work, we evaluate thermally, ex situ formed manganese oxide-coated cathodes for sodium chlorate production. The structure and morphology of the electrodes are investigated using various material characterization techniques, while the kinetic parameters of the HER is evaluated by electrochemical measurements. Finally, the hydrogen evolution selectivity is determined using mass spectrometry coupled with electrochemical measurements in an undivided electrochemical cell with solutions containing hypochlorite or chlorate.

MATERIALS AND METHODS

Chemicals Used. $Mn(NO_3)_2{\cdot}H_2O$, HCl (37%), NaOH, ethanol, NaCl, and NaClO solution (0.5 M in 0.1 M NaOH) were purchased from VWR International and were used as received. The recrystallized sodium chlorate ($NaClO_3$) was provided by Nouryon. The titanium substrates used in this study were supplied by Permascand AB.

The pH meter (Metrohm 827 pH lab or Metrohm 907 Titrando instruments, equipped with a Unitrode Pt 1000 combined pH and temperature sensor) was calibrated using commercial buffer solutions of pH 4.00 and 7.00 prior to each experiment. The pH values are reported as read from the instrument. Milli-Q grade water (ρ = 18.2 MΩ cm, from a Millipore Direct-Q3 UV instrument) was used to prepare all the solutions.

Electrode Preparation. Titanium disks (ϕ = 6 cm) were cleaned with a detergent solution, washed in water and ethanol, and subsequently etched in a boiling 1:1 mixture of 37% HCl and deionized water for 20 min. This step ensured the roughening of the surface and, hence, enhanced adhesion and mechanical stability of the deposited layers. The electrodes were rinsed with an excess amount of deionized water and ethanol and dried in air, and then Ti plates for reference measurements were put aside. To coat the remaining titanium plates, an approximate volume of 50 μL of ethanol-based 1 M $Mn(NO_3)_2$ solution was spread homogeneously using a short-haired brush. The electrodes were dried at T_1 = 60 °C for 10 min and subsequently annealed at T_2 = 200−500 °C for 10 min in a static furnace in an air atmosphere. The loading of the electrodes was controlled by the repetition of this coating cycle. As shown in Figure S1 of the Supporting Information (SI), the layer growth was continuous and linear, allowing control of the deposited MnO_x amount. After casting the last layer of the coating, the electrodes were annealed at T_2 for an extra 60 min to ensure the complete decomposition of the $Mn(NO_3)_2$ precursor.

For clarity, in the proceeding sections, the synthesis parameters of a given layer were not written at length. Instead, the electrodes were named according to the annealing temperature (T_2) and the MnO_x amount. For example, a layer formed at T_2 = 500 °C with 0.45 mg cm^{-2} MnO_x on the electrode was named MnO_x-500-0.45/Ti. For the current efficiency, cyclic voltammetry (CV), IR-corrected polarization curve, and electrochemical impedance spectroscopy (EIS) measurements, these electrodes were cut into A = 1 cm^2 sized disks, which were attached to Ti rods by spot-welding. The Ti rods were coated with a heat-shrinking tube (chemically resistant PVDF), and the backside and the sides of these electrodes were masked by epoxy resin.

Electrochemical Measurements. Cyclic voltammograms and EIS spectra of the electrodes were recorded using an Autolab 302N instrument equipped with an FRA32 module. The EIS spectra were recorded in the frequency range from 100 mHz to 100 kHz, using a 10 mV (RMS) sine wave perturbation.

The polarization curves were recorded using a Princeton Applied Research PAR273A instrument in galvanostatic mode, and the current-interruption technique was used to correct for the uncompensated IR-drop. The electrode was polarized at the given current density for 15 s, and the current was subsequently interrupted. The decay in potential was measured for 500 μs at a temporal resolution of Δt = 1 μs using a National Instrument NI-cdaq-9172 device.[45] The IR-corrected potential was determined by fitting a third-order polynomial to the experimental data. The measurements were performed at 10 current densities/decade, starting from the highest value (j = −100 mA cm^{-2}) and gradually decreasing it.

Current Efficiency Measurements. The current efficiency measurements were performed in a custom-designed electrochemical setup.[23] It consisted of a sealed, jacketed cell that had two openings on its tightly fitting lid, an inlet for the continuous (50 cm^3 min^{-1}) Ar gas purging (99.999% purity) and an outlet connected to the mass

DOI: 10.1021/acssuschemeng.9b01279
ACS Sustainable Chem. Eng. 2019, 7, 12170−12178

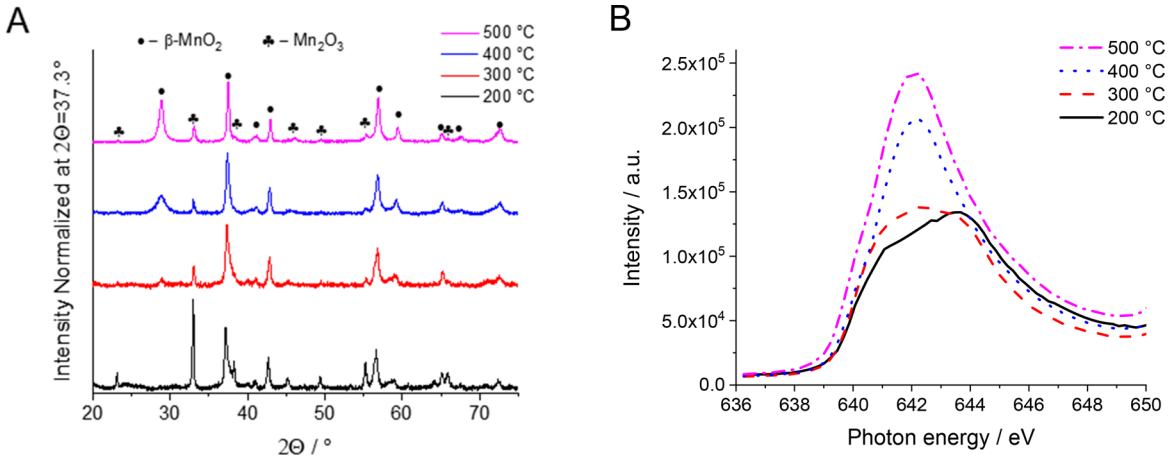

Figure 1. (A) XRD pattern and (B) NEXAFS spectra of the MnO_x samples formed from the thermal decomposition of $Mn(NO_3)_2$ at different annealing temperatures.

spectrometer (Hiden HPR-20) through a silica-gel-filled 20-cm-long gas-drying column. The pH of the solution was regulated using a Metrohm 907 Titrando titrator, with 2 M NaOH or 6 M HCl solutions. The temperature of the electrolyte was controlled by circulating water from an external heater bath in the jacket of the cell. Before each set of experiments, the instrument was calibrated by electrolyzing a 1 M NaOH solution between two platinum sheets at I = 300 mA. The H_2 production rate and the Faradaic efficiency values were calculated from the composition of the cell gas outlet. Except for the study of chlorate reduction at T = 70 °C, all the measurements were performed at room temperature (T = 22 ± 2 °C).

Physical Characterization of the Electrodes. X-ray diffraction (XRD) measurements were performed on a Rigaku MiniFlex 600 instrument, operating with a Cu Kα,1 radiation source (λ = 0.1541 nm). For the XRD measurements, the precursor was directly annealed in the oven at the same temperature as the electrodes, and the XRD pattern was recorded from the formed powders. Scanning electron microscopy (SEM) images were collected using a Hitachi S-4800 instrument at 20 kV accelerating voltage. Synchrotron radiation-X-ray photoelectron spectroscopy (SR-XPS) and near-edge X-ray absorption fine structure (NEXAFS) spectra were recorded on the Material Science Beamline at the Elettra synchrotron light source in Trieste, Italy.[46] The Mn 2p NEXAFS edge spectra were measured using Mn $L_3M_{45}M_{45}$ Auger electrons at about 635 eV (more precisely over a 625−640 eV range), noting that the inelastic mean free path (IMFP) of the detected Auger electrons, which is related to the escape depth and sampling depth of NEXAFS, is 2.4 nm at this electron energy with inorganic materials. Accordingly, the NEXAFS data pertain to the sample surface.

The calculation of the IMFP is immediate with eq 2 (for the A_i and B_i values, see Table 1 in the paper by Seah and Dench[47]):

$$\mathrm{IMPF}_i\ (\mathrm{nm}) = \frac{A_i}{E^2} + B_i E^{1/2} \qquad (2)$$

RESULTS AND DISCUSSION

XRD (Figure 1A) and NEXAFS (Figure 1B) measurements were performed to study the phase composition of the manganese oxides formed from the $Mn(NO_3)_2$ precursor at different annealing temperatures. On the basis of the XRD measurements (Figure 1A), the deposit formed at T_2 = 200 °C was identified as mostly Mn_2O_3 with a minor amount of β-MnO_2.[48,49] Note, however, that the presence of small amounts of manganese oxynitrates cannot be excluded.[50] At higher annealing temperatures, the Mn_2O_3 phase is still present, but the β-MnO_2 phase is the predominant species. The XRD patterns at the two highest annealing temperatures are very similar, indicating a similar phase composition in both cases. The only significant difference between these temperatures is the sharpness of the Bragg reflections with the samples annealed at 500 °C. This indicates that the average crystallite size increases with the increasing annealing temperature (from ∼9 to ∼14 nm, calculated from the Scherrer equation from the reflection at 2Θ = 28.8°).

The NEXAFS measurements (Figure 1B), which—unlike the bulk analysis technique of crystalline phases by XRD—provided surface compositional data of both noncrystalline and crystalline materials within the top few nanometers of the samples, yielded a different picture. At lower annealing temperatures, the +4 oxidation state of manganese is the dominant surface species as determined from the peak positions and the shape of the spectrum (a convolution of partially resolved major peaks at 641, 642, and 643.5 eV), while mixtures of +3/+4 oxidation states were evidenced for the samples formed at 300−500 °C (a mixture of major peaks at 640, 641.5, and 642.5 eV along with those at 641, 642, and 643.5 eV).[51]

This can be attributed to the formation of Mn_2O_3 from the thermal decomposition of MnO_2 on the electrode surface at higher temperatures. It is important to note that Liu et al.[52] used differential scanning calorimetry (DSC) coupled to XRD to show that there is some thermal decomposition of MnO_2 to Mn_2O_3 between 450 and 550 °C, and given that the present bulk XRD and surface NEXAFS data of our materials revealed MnO_2 and Mn_2O_3, respectively, under these conditions, it is likely that thermal decomposition is restricted to the surface of the MnO_x films. In line with this, the SR-XPS surface compositions of samples yielded O-to-Mn atomic ratios of 1.98 for the electrodes formed at 200 °C (MnO_2) and approximately 1.75 (mixtures of Mn_2O_3 and MnO_2) at higher temperatures (Table S1, SI), as observed using photon-energy-dependent photoabsorption parameters and kinetic-energy-dependent SR-XPS factors (Figure S2A−D, SI).[53] In the sample formed at 200 °C, the presence of NO_3^- from the $Mn(NO_3)_2$ precursor residues was proven by a N 1s peak for NO_3^- at 406.5 eV (Figure S3, SI).[54] Furthermore, all the SR-XPS O 1s spectra (Figure S4A−D, SI) had peaks at 529.5 eV (O^{2-}), 531.5 eV (OH^-), and 533.0 eV (H_2O),[54] showing the presence of small amounts of $Mn(OH)_x$ phases such as MnO(OH) and/or $Mn(OH)_2$ and/or $Mn(OH)_4$.

DOI: 10.1021/acssuschemeng.9b01279
ACS Sustainable Chem. Eng. 2019, 7, 12170−12178

At a lower annealing temperature, a structure with larger holes is formed, which becomes more compact at higher annealing temperatures (Figure 2). For the electrodes formed

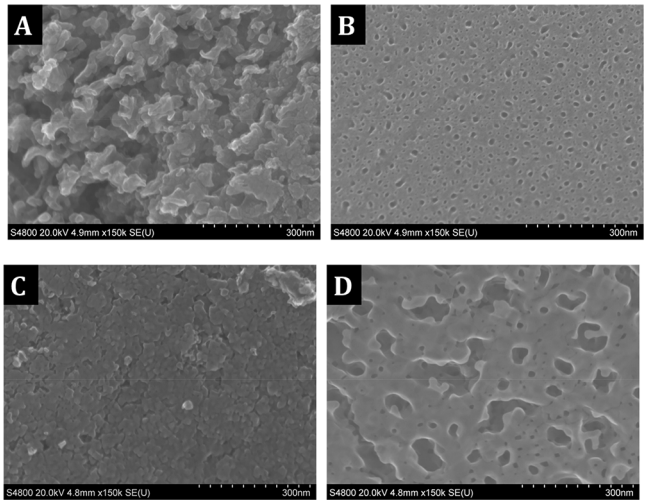

Figure 2. SEM images taken of the MnO_x/Ti electrodes formed at different annealing temperatures of (A) T_2 = 200 °C, (B) T_2 = 300 °C, (C) T_2 = 400 °C, (D) T_2 = 500 °C, with the same MnO_x loading (~1.5 mg cm^{-2}).

at 400 °C, an almost coherent surface is observed, assembled from 10−30 nm large nanoparticles. As the annealing temperature is further increased, the interface between the individual nanoparticles disappears and the nanoparticles melt together to form a coherent layer with larger holes. Importantly, irrespective of the annealing temperature of the samples, no significant differences can be observed along the layer, even at larger areas (for low magnification, see Figure S5, SI).

The different morphology, and hence an electrochemically active surface area (ECSA), is reflected in the double-layer capacitance of the electrodes, as shown in Figure S6A (SI). While the ECSA (directly related to the current) is comparable for the electrodes formed at 200−400 °C, it appears to be significantly smaller in the case of the electrode annealed at 500 °C. The qualitative analysis of the EIS spectra (Figure S6B, SI) of this electrode at high frequencies, however, indicates its porous nature.[55]

The HER activity of the films was tested by recording IR-corrected polarization curves (Figure 3). As compared to a bare Ti electrode, the potential of HER read at j = −1 mA cm^{-2} is ~100 mV more negative on the manganese oxide-coated electrodes. By contrast, the Tafel slope was about 130−140 mV $decade^{-1}$ with the MnO_x electrodes, while it was 240 mV $decade^{-1}$ with the titanium electrode. From the interplay of these two factors, a less-negative potential is required at an industrially relevant current density of j = −100 mA cm^{-2} to drive HER on the coated electrodes, irrespective of the annealing temperature. Interestingly, the large difference in the ECSA (Figure S6A,B, SI) of the MnO_x-coated electrodes is not reflected in the high current density range of the polarization curves, where the potentials for the different electrodes are similar.

Starting the polarization curve measurements at the most negative potential resulted in a reduction of the MnO_x films. As the potential reaches the value of E = −1.55 V, the films are

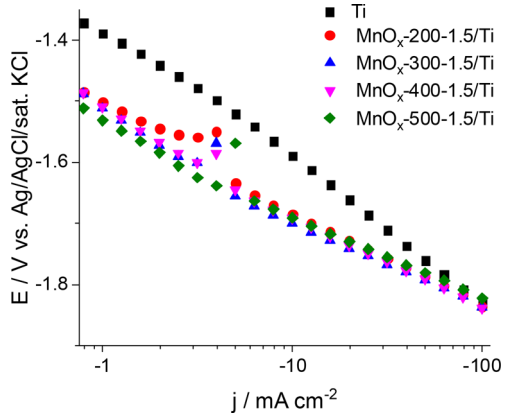

Figure 3. IR-corrected polarization curves with a bare Ti electrode and MnO_x/Ti electrodes prepared at different annealing temperatures with an identical MnO_x loading (1.5 mg cm^{-2}). The measurements were performed in N_2-purged 2 M NaCl solution.

oxidized; this potential has been reported to correspond to the Mn(II) to Mn(II/III) oxidation.[56] The irregular behavior of the polarization curves in that potential region for the MnO_x-covered electrodes may be related to the mentioned oxidation reaction. All films show this behavior, which indicates that the films, independent of the initial composition, are reduced to the same oxidation state [Mn(II)] under polarization, suggesting that the composition of the films is similar under operation. However, no in situ analyses of the electrodes were made to prove this assumption.

Polarization curves with electrodes coated with different MnO_x amounts (Figure S7, SI) showed that at low loadings the electrochemical properties of the electrodes closely resembled those of the Ti plate. At higher coating amounts, no significant difference can be seen between the recorded polarization curves. This indicates that the coating thickness, in the studied range, has no major influence on the energy efficiency of the electrolysis process in the −100−300 mA cm^{-2} current density range, which is important for practical application. Note that at higher MnO_x loadings (above 4 mg cm^{-2}) we experienced cracking of the MnO_x-coated electrodes, and therefore, no electrochemical measurements were performed using these.

The HER selectivity with the MnO_x-coated and bare Ti electrodes in hypochlorite solutions was evaluated by galvanostatic measurements (Figure 4). In such an experiment, the H_2 content of the cell gas outlet was continuously monitored during electrolysis (at j = −100, −200, −300 mA cm^{-2}, each for 20 min). As shown in Figure 4A, the H_2 production rate continuously increases with the current density for both a reference Ti plate and a typical MnO_x-coated electrode. It is important to note that the HER efficiency (Figure 4B), calculated as the ratio of the measured and the maximum theoretical H_2 production rate, increases with the current density for all the studied electrodes, even for the Ti plate. The reason behind this is that under these experimental conditions the rate of electrochemical hypochlorite reduction is limited by the mass transport of these species.[23] Hence, the partial current density for hypochlorite reduction is the same at all applied current densities, leading to a decreasing Faraday efficiency loss (the ratio of the partial current density for hypochlorite reduction and the total current density) at higher current densities.

DOI: 10.1021/acssuschemeng.9b01279
ACS Sustainable Chem. Eng. 2019, 7, 12170−12178

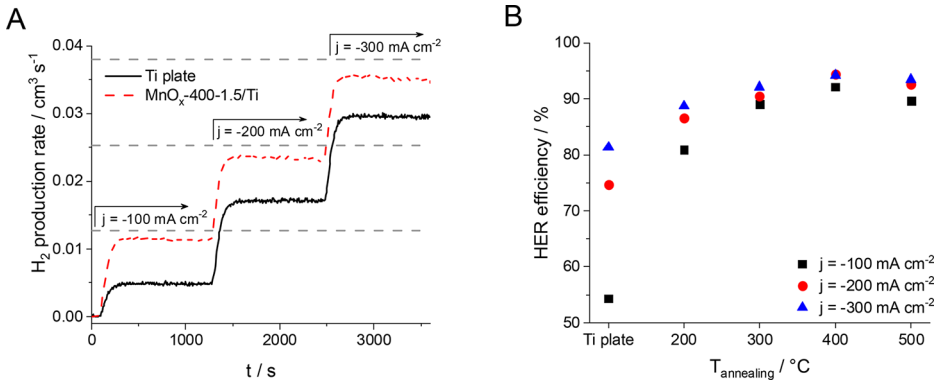

Figure 4. (A) Hydrogen production rate during the electrolysis in an 80 mM NaClO + 2 M NaCl solution (pH 6.5, room temperature) using an A = 1 cm^2 Ti plate or a MnO_x-400-1.5/Ti electrode at different current densities (each for 1200 s). The dashed lines show the theoretical maximum H_2 production rate at the different current densities (Faraday's law, 100% HER efficiency). (B) The HER efficiency during measurements identical to those shown in part A, as a function of annealing temperature of MnO_x/Ti electrodes with 1.5 mg cm^{-2} MnO_x loading.

Comparing the results with a MnO_x-covered electrode to a bare Ti plate, a significantly higher H_2 production rate was observed at each applied current density (Figure 4A). Quantifying the HER efficiency at a fixed MnO_x loading (i.e., 1.5 mg cm^{-2}), but with electrodes formed at different annealing temperatures, the highest value was achieved with the layers formed at T_2 = 400 °C, but the layers formed at higher annealing temperatures showed similar results (Figure 4B). This dependency is dictated by the interplay of several factors, such as the initial phase composition and the morphology of the electrodes, which in turn is determined by the annealing temperature. The main impact of annealing temperature might be the sintering of particles in the film resulting in a more coherent structure.

The electrochemical reduction of chlorate, another cathodic loss reaction during chlorate production, was also evaluated (Figure 5) on the MnO_x-coated electrodes. The HER

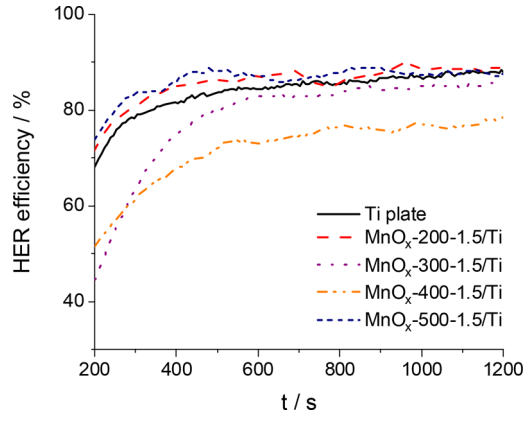

Figure 5. HER efficiency at j = −300 mA cm^{-2} on Ti and MnO_x/Ti electrodes (1.5 mg cm^{-2} MnO_x amount) in 5.2 M $NaClO_3$ solution at pH ≈7 and T = 70 °C.

efficiency remained at around 85−86% with a Ti electrode at high temperature in a high ionic strength chlorate solution. As was the case with the hypochlorite reduction reaction, the annealing temperature had a significant influence on the electrochemical behavior of the manganese oxide electrodes. Interestingly, the trend is almost reversed in this case; a lower HER efficiency was found with layers formed at 300 and 400 °C, while it is slightly higher compared to a Ti electrode with samples prepared at 200 and 500 °C. It should be emphasized that the electrodes remained stable in both hypochlorite and chlorate solutions, exhibiting no signs of either physical or oxidative degradation during the time frames of the measurements.

It is worth mentioning that the current efficiency improvement upon coating the Ti electrodes with MnO_x was significantly smaller when studying the electrochemical reduction of chlorate ions compared with the case of hypochlorite. We believe that this difference is rooted in the distinct mechanism of the two electrochemical processes; hypochlorite reduction requires very little driving force (overpotential), and therefore, its rate is limited by mass transport under industrial circumstances. On the other hand, the reduction of chlorate is an activation-controlled process, requiring a significantly larger overpotential or the application of well-designed, catalytic electrodes.[57] Further, the different permeability of the MnO_x layer for hypochlorite and chlorate ions of very different size may also be an important factor.

As these samples revealed the most promising results, the electrodes annealed at T_2 = 400 and 500 °C were evaluated in further experiments.

The HER efficiency in hypochlorite solution was quantified with electrodes formed at T_2 = 400 or 500 °C at different loadings, hence thicknesses, of MnO_x (parts A and B of Figure 6, respectively). For the electrodes formed at 400 °C, the Faradaic efficiency scaled continuously with the MnO_x amount up to the level of 1.5 mg cm^{-2} (∼2−3 μm thickness), with a slight decrease upon further thickening the film. Similarly, a thickness-dependent HER efficiency can be seen with samples annealed at 500 °C, but no decrease was noted for the thicker electrodes, and the HER efficiency remained constant at higher MnO_x amounts under the conditions of this study. Importantly, a HER efficiency of ca. 95% (∼82% on a control Ti plate) was achieved with the best-performing electrodes at both annealing temperatures. The increase in HER efficiency with the thicker electrodes can be attributed to a more homogeneous and continuous coverage on the titanium substrate, as supported by the recorded SEM images (Figure S8A−F, SI). In general, it is expected to be a maximum in optimal thickness, as too thick films may lead to cracks during annealing due to differences in temperature expansion coefficients between the film material and the substrate.

DOI: 10.1021/acssuschemeng.9b01279
ACS Sustainable Chem. Eng. 2019, 7, 12170−12178

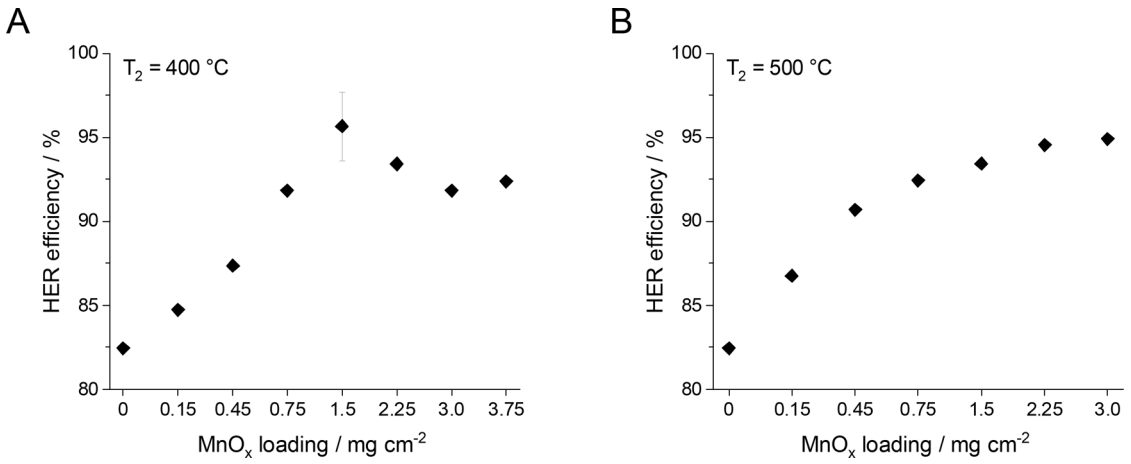

Figure 6. HER efficiency at $j = -300$ mA cm^{-2} as a function of the MnO_x loading during electrolysis in an 80 mM NaClO + 2 M NaCl solution (pH 6.5, room temperature) for layers annealed at (A) $T_2 = 400$ °C and (B) $T_2 = 500$ °C.

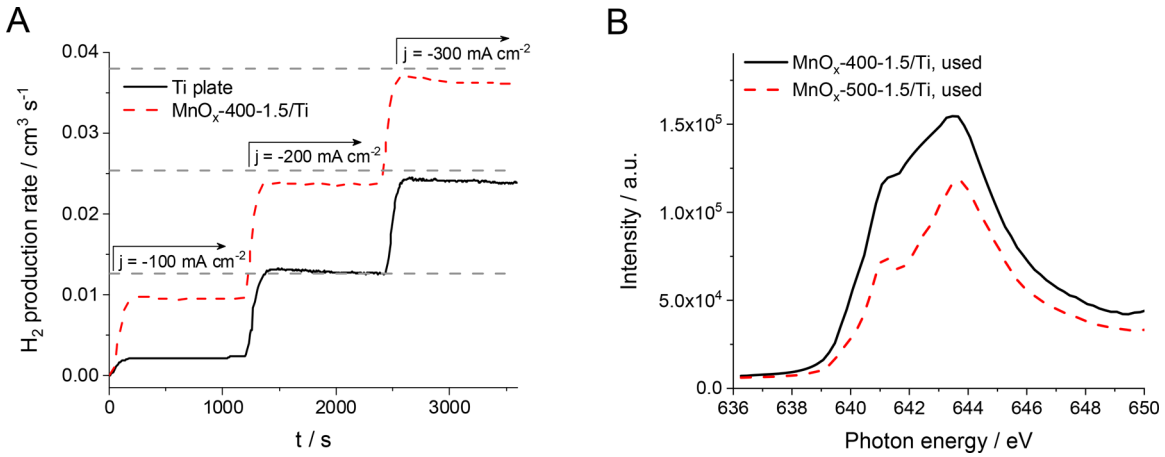

Figure 7. (A) H_2 production rate during electrolysis at different current densities ($j = -100$, -200, and -300 mA cm^{-2}) on MnO_x-400-1.5/Ti and Ti electrodes in an 80 mM NaClO + 2 M NaCl solution at pH 12 and $T = 80$ °C. The dashed lines show the maximum H_2 production rate (Faraday's law, 100% HER efficiency). (B) NEXAFS spectra of electrodes formed at 400 and 500 °C, after subjecting them to electrochemical polarization in hypochlorite solution.

As the industrial use of such electrodes demands their applicability at elevated temperature, the HER selectivity of the manganese oxide layers was also evaluated in $T = 80$ °C hypochlorite solution, which is shown herein for an MnO_x-400-1.5/Ti electrode as an example (Figure 7A). Note that for these measurements the solution pH was kept at pH 12 to avoid the rapid homogeneous decomposition of hypochlorite.[15] An alkaline pH is also representative of the electrolyte close to a chlorate cathode, where the hydroxide ions produced during hydrogen evolution cause increased local pH. The conclusions from these measurements are identical to those derived at lower solution temperatures (Figure 4); with MnO_x-coated electrodes the HER efficiency was above 95% at $j = -300$ mA cm^{-2}, as compared to ~65% on a control Ti plate. Again, there was no sign of degradation during electrochemical measurements, not even after prolonged exposure of the electrodes to a warm (80 °C) hypochlorite solution. To emphasize this point, the electrode composition was studied by NEXAFS after electrochemical polarization in hypochlorite solution. As seen in Figure 7B, the NEXAFS spectra of the films formed at 400 and 500 °C are very similar after exposing these electrodes to hypochlorite, showing an almost exclusive +4 oxidation state of manganese (see +4 peaks at 641, 642, and 643.5 eV).[51] Furthermore, these samples yielded SR-XPS-determined O-to-Mn atomic ratios of 2.0−2.2 and a major O 1s peak at 529.5 eV due to O^{2-},[54] which are also indicative of the exclusive presence of MnO_2 on the electrode surface under these conditions. This shows that the layers are partially oxidized upon exposure to hypochlorite. Note, however, that there were no observations of higher oxidation states in the NEXAFS spectra (nor could we observe any purple coloration of the electrolyte, which would indicate the oxidative dissolution of the manganese oxide layers). This shows that the formed MnO_2 phase is stable under the studied conditions.

Comparing the results herein presented to our earlier studies,[23] we can conclude that both amorphous and crystalline MnO_x coatings lead to similarly increased HER selectivity in hypochlorite solutions. However, in the present case, mechanically stable electrodes were formed by an easily scalable method, which is a prerequisite for industrial application.

CONCLUSIONS

Manganese oxide-coated titanium cathodes were formed by thermal decomposition of a $Mn(NO_3)_2$ precursor. The morphology and phase composition of the coatings were

DOI: 10.1021/acssuschemeng.9b01279
ACS Sustainable Chem. Eng. 2019, 7, 12170−12178

controlled by the annealing temperature of the samples, as proven by various materials characterization techniques, including synchrotron radiation X-ray absorption and photoelectron spectroscopies. By coating the titanium electrode with such manganese oxide layers, the hydrogen evolution reaction selectivity significantly increased in hypochlorite solutions, without notable difference in the cell voltage. The best results were found for the layers formed at 400 and 500 °C; in both cases, the hydrogen evolution reaction selectivity was above 95% (as compared to 78% on a titanium electrode). As for the latter, the rate of chlorate reduction was also comparably low. Furthermore, the formed layers were stable, even after prolonged exposure to hot hypochlorite solutions. Such manganese oxide-coated electrodes therefore represent a very attractive group of selective cathodes for the industrial production of sodium chlorate. Since they are the first reported ex-situ-coated chromium-free cathodes for the chlorate process with increased current efficiency, further investigations under more industrially relevant conditions are planned.

■ ASSOCIATED CONTENT

Supporting Information

The Supporting Information is available free of charge on the ACS Publications website at DOI: 10.1021/acssuschemeng.9b01279.

Further information on electrode preparation and the morphology (SEM), phase composition (SR-XPS), and electrochemical properties of the manganese oxide-coated electrodes (PDF)

■ AUTHOR INFORMATION

Corresponding Authors

*E-mail: endrodib@chem.u-szeged.hu (B.E.).
*E-mail: amco@kth.se (A.C.).

ORCID

Balázs Endrődi: 0000-0003-3237-9222
Maria Cuartero: 0000-0002-3858-8466
Roland de Marco: 0000-0002-1357-3727
Gaston A. Crespo: 0000-0002-1221-3906
Ann Cornell: 0000-0001-5816-2924

Notes

The authors declare no competing financial interest.

■ ACKNOWLEDGMENTS

The assistance of Hyeyun Kim with taking the SEM images, as well as John Bradley and Raymart Walker with the SR-XPS and NEXAFS measurements, is gratefully acknowledged. The authors would like to express their gratitude to Ramcon for providing a Rigaku MiniFlex 600 instrument for the XRD measurements. We thank Permascand AB for supplying the titanium substrates used in this study. The financial support from the Swedish Energy Agency, Permascand, and Nouryon is gratefully acknowledged. We are grateful for the support of the European Community's Seventh Framework Programme (FP7/2007-2013) under grant agreement no 312284 for the research that was conducted on the Materials Science Beamline (MSB) at the Elettra Synchrotron. The CERIC-ERIC Consortium for access to experimental facilities and financial support, the CERIC-ERIC consortium and Czech Ministry of Education (LM2015057) are also acknowledged for financial support. We pay special acknowledgement to Drs. Nataliya Tsud and Kevin C. Prince at the Elettra Synchrotron for assistance with the experiments. M.C. and G.A.C. acknowledge the CERIC users' grant, while RDM thanks the International Synchrotron Access Program (ISAP) of the Australian Synchrotron for travel funding to attend the experiment at the Elettra Synchrotron.

■ REFERENCES

(1) Endrődi, B.; Simic, N.; Wildlock, M.; Cornell, A. A Review of Chromium(VI) Use in Chlorate Electrolysis: Functions, Challenges and Suggested Alternatives. *Electrochim. Acta* **2017**, *234*, 108−122.

(2) Jung, Y. J.; Baek, K. W.; Oh, B. S.; Kang, J.-W. An Investigation of the Formation of Chlorate and Perchlorate during Electrolysis Using Pt/Ti Electrodes: The Effects of PH and Reactive Oxygen Species and the Results of Kinetic Studies. *Water Res.* **2010**, *44* (18), 5345−5355.

(3) Yoon, Y.; Cho, E.; Jung, Y.; Kwon, M.; Yoon, J.; Kang, J.-W. Evaluation of the Formation of Oxidants and By-Products Using Pt/Ti, RuO_2/Ti, and IrO_2/Ti Electrodes in the Electrochemical Process. *Environ. Technol.* **2015**, *36* (3), 317−326.

(4) Neodo, S.; Rosestolato, D.; Ferro, S.; De Battisti, A. On the Electrolysis of Dilute Chloride Solutions: Influence of the Electrode Material on Faradaic Efficiency for Active Chlorine, Chlorate and Perchlorate. *Electrochim. Acta* **2012**, *80*, 282−291.

(5) Hernlem, B. J. Electrolytic Destruction of Urea in Dilute Chloride Solution Using DSA Electrodes in a Recycled Batch Cell. *Water Res.* **2005**, *39* (11), 2245−2252.

(6) Cornell, A.; Lindbergh, G.; Simonsson, D. The Effect of Addition of Chromate on the Hydrogen Evolution Reaction and on Iron Oxidation in Hydroxide and Chlorate Solutions. *Electrochim. Acta* **1992**, *37* (10), 1873−1881.

(7) Ahlberg Tidblad, A.; Lindbergh, G. Surface Analysis with ESCA and GD-OES of the Film Formed by Cathodic Reduction of Chromate. *Electrochim. Acta* **1991**, *36* (10), 1605−1610.

(8) Lindbergh, G.; Simonsson, D. Inhibition of Cathode Reactions in Sodium Hydroxide Solution Containing Chromate. *Electrochim. Acta* **1991**, *36* (13), 1985−1994.

(9) Lindbergh, G.; Simonsson, D. The Effect of Chromate Addition on Cathodic Reduction of Hypochlorite in Hydroxide and Chlorate Solutions. *J. Electrochem. Soc.* **1990**, *137* (10), 3094.

(10) Tidblad, A. A.; Martensson, J. In Situ Ellipsometric Characterization of Films Formed by Cathodic Reduction of Chromate. *Electrochim. Acta* **1997**, *42* (3), 389−398.

(11) Ball, J. W.; Nordstrom, D. K. Critical Evaluation and Selection of Standard State Thermodynamic Properties for Chromium Metal and Its Aqueous Ions, Hydrolysis Species, Oxides, and Hydroxides. *J. Chem. Eng. Data* **1998**, *43* (6), 895−918.

(12) Spasojević, M.; Marković, D.; Trišović, T.; Spasojević, M. Mathematical Model of the Catalytic Effect of Chromium(VI) on Hypochlorite Disproportionation in Chlorate Electrolysis. *J. Electrochem. Soc.* **2018**, *165* (2), E8−E19.

(13) Wanngård, J.; Wildlock, M. The Catalyzing Effect of Chromate in the Chlorate Formation Reaction. *Chem. Eng. Res. Des.* **2017**, *121*, 438−447.

(14) Kalmár, J.; Szabó, M.; Simic, N.; Fábián, I. Kinetics and Mechanism of the Chromium(VI) Catalyzed Decomposition of Hypochlorous Acid at Elevated Temperature and High Ionic Strength. *Dalt. Trans.* **2018**, *47* (11), 3831−3840.

(15) Endrődi, B.; Sandin, S.; Wildlock, M.; Simic, N.; Cornell, A. Suppressed Oxygen Evolution during Chlorate Formation from Hypochlorite in the Presence of Chromium(VI). *J. Chem. Technol. Biotechnol.* **2019**, *94* (5), 1520−1527.

(16) European Chemicals Agency (ECHA). Authorization List (Annex XIV of REACH). 2015. https://echa.europa.eu/authorisation-list (accessed June 21, 2019).

(17) Vogt, H. Electrosynthesis of Chlorate in the Nineteenth Century. *J. Electrochem. Soc.* **1981**, *128* (2), 29C.

DOI: 10.1021/acssuschemeng.9b01279
ACS Sustainable Chem. Eng. 2019, 7, 12170−12178

(18) Kuhn, A. T.; Hamzah, H.; Collins, G. C. S. The Inhibition of the Cathodic Reduction of Hypochlorite by Films Deposited at the Cathode Surface. *J. Chem. Technol. Biotechnol.* **1980**, *30* (1), 423−428.
(19) Gustavsson, J.; Nylén, L.; Cornell, A. Rare Earth Metal Salts as Potential Alternatives to Cr(VI) in the Chlorate Process. *J. Appl. Electrochem.* **2010**, *40* (8), 1529−1536.
(20) Li, M.; Twardowski, Z.; Mok, F.; Tam, N. Sodium Molybdate—a Possible Alternate Additive for Sodium Dichromate in the Electrolytic Production of Sodium Chlorate. *J. Appl. Electrochem.* **2007**, *37* (4), 499−504.
(21) Gustavsson, J.; Li, G.; Hummelgard, C.; Backstrom, J.; Cornell, A. On the Suppression of Cathodic Hypochlorite Reduction by Electrolyte Additions of Molybdate and Chromate Ions. *J. Electrochem. Sci. Eng.* **2012**, *2*, 185−198.
(22) Gustavsson, J.; Hummelgard, C.; Backstrom, J.; Wallinder, I. O.; Rahman, S. M.; Lindbergh, G.; Eriksson, S.; Cornell, A. In-Situ Activated Hydrogen Evolution by Molybdate Addition to Neutral and Alkaline Electrolytes. *J. Electrochem. Sci. Eng.* **2012**, *2* (3), 105−120.
(23) Endrődi, B.; Sandin, S.; Smulders, V.; Simic, N.; Wildlock, M.; Mul, G.; Mei, B. T.; Cornell, A. Towards Sustainable Chlorate Production: The Effect of Permanganate Addition on Current Efficiency. *J. Cleaner Prod.* **2018**, *182*, 529−537.
(24) Endrődi, B.; Smulders, V.; Simic, N.; Wildlock, M.; Mul, G.; Mei, B.; Cornell, A. In Situ Formed Vanadium-Oxide Cathode Coatings for Selective Hydrogen Production. *Appl. Catal., B* **2019**, *244*, 233−239.
(25) Gomes, A. S. O.; Busch, M.; Wildlock, M.; Simic, N.; Ahlberg, E. Understanding Selectivity in the Chlorate Process: A Step towards Efficient Hydrogen Production. *ChemistrySelect* **2018**, *3* (23), 6683−6690.
(26) Yoshida, M.; Takanabe, K.; Maeda, K.; Ishikawa, A.; Kubota, J.; Sakata, Y.; Ikezawa, Y.; Domen, K. Role and Function of Noble-Metal/Cr-Layer Core/Shell Structure Cocatalysts for Photocatalytic Overall Water Splitting Studied by Model Electrodes. *J. Phys. Chem. C* **2009**, *113* (23), 10151−10157.
(27) Maeda, K.; Teramura, K.; Lu, D.; Saito, N.; Inoue, Y.; Domen, K. Noble-Metal/Cr_2O_3 Core/Shell Nanoparticles as a Cocatalyst for Photocatalytic Overall Water Splitting. *Angew. Chem., Int. Ed.* **2006**, *45* (46), 7806−7809.
(28) Maeda, K.; Teramura, K.; Lu, D.; Saito, N.; Inoue, Y.; Domen, K. Roles of Rh/Cr_2O_3 (Core/Shell) Nanoparticles Photodeposited on Visible-Light-Responsive (Ga1- XZn x)(N 1- x O x) Solid Solutions in Photocatalytic Overall Water Splitting. *J. Phys. Chem. C* **2007**, *111* (20), 7554−7560.
(29) Qureshi, M.; Shinagawa, T.; Tsiapis, N.; Takanabe, K. Exclusive Hydrogen Generation by Electrocatalysts Coated with an Amorphous Chromium-Based Layer Achieving Efficient Overall Water Splitting. *ACS Sustainable Chem. Eng.* **2017**, *5* (9), 8079−8088.
(30) Esposito, D. V. Membrane-Coated Electrocatalysts—An Alternative Approach To Achieving Stable and Tunable Electrocatalysis. *ACS Catal.* **2018**, *8* (1), 457−465.
(31) Hedenstedt, K.; Gomes, A. S. O.; Busch, M.; Ahlberg, E. Study of Hypochlorite Reduction Related to the Sodium Chlorate Process. *Electrocatalysis* **2016**, *7* (4), 326−335.
(32) Dincer, I. Green Methods for Hydrogen Production. *Int. J. Hydrogen Energy* **2012**, *37* (2), 1954−1971.
(33) Dincer, I.; Acar, C. Review and Evaluation of Hydrogen Production Methods for Better Sustainability. *Int. J. Hydrogen Energy* **2015**, *40* (34), 11094−11111.
(34) El-Moneim, A. A.; Bhattarai, J.; Kato, Z.; Izumiya, K.; Kumagai, N.; Hashimoto, K. Mn-Mo-Sn Oxide Anodes for Oxygen Evolution in Seawater Electrolysis for Hydrogen Production. *ECS Trans.* **2009**, *25*, 127−137.
(35) El-Moneim, A. A.; Kumagai, N.; Hashimoto, K. Mn-Mo-W Oxide Anodes for Oxygen Evolution in Seawater Electrolysis for Hydrogen Production. *Mater. Trans.* **2009**, *50* (8), 1969−1977.
(36) Fujimura, K.; Izumiya, K.; Kawashima, A.; Akiyama, E.; Habazaki, H.; Kumagai, N.; Hashimoto, K. Anodically Deposited Manganese-Molybdenum Oxide Anodes with High Selectivity for Evolving Oxygen in Electrolysis of Seawater. *J. Appl. Electrochem.* **1999**, *29* (6), 769−775.
(37) Abdel Ghany, N.; Kumagai, N.; Meguro, S.; Asami, K.; Hashimoto, K. Oxygen Evolution Anodes Composed of Anodically Deposited Mn−Mo−Fe Oxides for Seawater Electrolysis. *Electrochim. Acta* **2002**, *48* (1), 21−28.
(38) Hashimoto, K.; El-Moneim, A. A.; Kumagai, N.; Asami, K. New Nanocrystalline Manganese-Molybdenum-Tin Oxide Anodes for Oxygen Evolution in Seawater Electrolysis. *ECS Trans.* **2005**, *1*, 491−497.
(39) Habazaki, H.; Matsui, T.; Kawashima, A.; Asami, K.; Kumagai, N.; Hashimoto, K. Nanocrystalline Manganese-Molybdenum-Tungsten Oxide Anodes for Oxygen Evolution in Seawater Electrolysis. *Scr. Mater.* **2001**, *44* (8−9), 1659−1662.
(40) Fujimura, K.; Matsui, T.; Izumiya, K.; Kumagai, N.; Akiyama, E.; Habazaki, H.; Kawashima, A.; Asami, K.; Hashimoto, K. Oxygen Evolution on Manganese−Molybdenum Oxide Anodes in Seawater Electrolysis. *Mater. Sci. Eng., A* **1999**, *267* (2), 254−259.
(41) Izumiya, K.; Akiyama, E.; Habazaki, H.; Kumagai, N.; Kawashima, A.; Hashimoto, K. Effects of Additional Elements on Electrocatalytic Properties of Thermally Decomposed Manganese Oxide Electrodes for Oxygen Evolution from Seawater. *Mater. Trans., JIM* **1997**, *38* (10), 899−905.
(42) Bennett, J. E. Electrodes for Generation of Hydrogen and Oxygen from Seawater. *Int. J. Hydrogen Energy* **1980**, *5* (4), 401−408.
(43) Balaji, R.; Kannan, B. S.; Lakshmi, J.; Senthil, N.; Vasudevan, S.; Sozhan, G.; Shukla, A. K.; Ravichandran, S. An Alternative Approach to Selective Sea Water Oxidation for Hydrogen Production. *Electrochem. Commun.* **2009**, *11* (8), 1700−1702.
(44) Vos, J. G.; Wezendonk, T. A.; Jeremiasse, A. W.; Koper, M. T. M. MnO_x/IrO_x as Selective Oxygen Evolution Electrocatalyst in Acidic Chloride Solution. *J. Am. Chem. Soc.* **2018**, *140* (32), 10270−10281.
(45) Hummelgård, C.; Karlsson, R. K. B.; Bäckström, J.; Rahman, S. M. H.; Cornell, A.; Eriksson, S.; Olin, H. Physical and Electrochemical Properties of Cobalt Doped (Ti,Ru)O_2 Electrode Coatings. *Mater. Sci. Eng., B* **2013**, *178* (20), 1515−1522.
(46) Cuartero, M.; Acres, R. G.; Jarolímová, Z.; Bakker, E.; Crespo, G. A.; De Marco, R. Electron Hopping between Fe 3 d States in Ethynylferrocene-Doped Poly(Methyl Methacrylate)-Poly(Decyl Methacrylate) Copolymer Membranes. *Electroanalysis* **2018**, *30* (4), 596−601.
(47) Seah, M. P.; Dench, W. A. Quantitative Electron Spectroscopy of Surfaces: A Standard Data Base for Electron Inelastic Mean Free Paths in Solids. *Surf. Interface Anal.* **1979**, *1* (1), 2−11.
(48) Gao, T.; Fjellvåg, H.; Norby, P. A Comparison Study on Raman Scattering Properties of α- and β-MnO2. *Anal. Chim. Acta* **2009**, *648* (2), 235−239.
(49) Zhang, J.; Li, Y.; Wang, L.; Zhang, C.; He, H. Catalytic Oxidation of Formaldehyde over Manganese Oxides with Different Crystal Structures. *Catal. Sci. Technol.* **2015**, *5* (4), 2305−2313.
(50) De Bruijn, T. J. W.; De Jong, W. A.; Van Den Berg, P. J. Thermal Decomposition of Aqueous Manganese Nitrate Solutions and Anhydrous Manganese Nitrate. Part 1. Mechanism. *Thermochim. Acta* **1981**, *45* (3), 265−278.
(51) Mette, K.; Bergmann, A.; Tessonnier, J.-P.; Hävecker, M.; Yao, L.; Ressler, T.; Schlögl, R.; Strasser, P.; Behrens, M. Nanostructured Manganese Oxide Supported on Carbon Nanotubes for Electrocatalytic Water Splitting. *ChemCatChem* **2012**, *4* (6), 851−862.
(52) Liu, B.; Thomas, P. S.; Ray, A. S.; Williams, R. P. The Effect of Sampling Conditions on the Thermal Decomposition of Electrolytic Manganese Dioxide. *J. Therm. Anal. Calorim.* **2004**, *76* (1), 115−122.
(53) Cuartero, M.; Bishop, J.; Walker, R.; Acres, R. G.; Bakker, E.; De Marco, R.; Crespo, G. A. Evidence of Double Layer/Capacitive Charging in Carbon Nanomaterial-Based Solid Contact Polymeric Ion-Selective Electrodes. *Chem. Commun.* **2016**, *52* (62), 9703−9706.
(54) Chastain, J.; King, R. C.; Moulder, J. *Handbook of X-ray Photoelectron Spectroscopy: A Reference Book of Standard Spectra for*

DOI: 10.1021/acssuschemeng.9b01279
ACS Sustainable Chem. Eng. 2019, 7, 12170−12178

Identification and Interpretation of XPS Data; Physical Electronics Division, Perkin-Elmer Corp.: Eden Prairie, MN, 1992.
(55) Raistrick, I. D. Impedance Studies of Porous Electrodes. *Electrochim. Acta* **1990**, *35* (10), 1579−1586.
(56) Djurfors, B.; Broughton, J. N.; Brett, M. J.; Ivey, D. G. Electrochemical Oxidation of Mn/MnO Films: Mechanism of Porous Film Growth. *J. Electrochem. Soc.* **2006**, *153* (1), A64.
(57) Tilak, B. V. Metal Anodes and Hydrogen Cathodes: Their Activity Towards O2 Evolution and ClO3− Reduction Reactions. *J. Electrochem. Soc.* **1988**, *135* (6), 1386.

DOI: 10.1021/acssuschemeng.9b01279
ACS Sustainable Chem. Eng. 2019, 7, 12170−12178